Materials Today Bio 18 (2023) 100532

Contents lists available at ScienceDirect

Materials Today Bio

journal homepage: www.journals.elsevier.com/materials-today-bio

# Drug-independent NADPH-consuming micelles collaborate with ROS-generator for cascade ferroptosis amplification by impairing redox homeostasis

Fangying Yu [a,1], Xuwei Shang [a,1], Zixu Wang [a], Yun Zhu [b], Simin Chen [a], Hong Yuan [a], Fuqiang Hu [a,*]

[a] College of Pharmaceutical Science, Zhejiang University, 866 Yuhangtang Road, Hangzhou, 310058, People's Republic of China
[b] Department of Pharmacy, Nanjing Drum Tower Hospital, The Affiliated Hospital of Nanjing University Medical School, Nanjing, Jiangsu, 210008, China

ARTICLE INFO

*Keywords:*
NADPH consumption
ROS generator
Cascade ferroptosis amplification
Redox homeostasis

ABSTRACT

Ferroptosis as promising antitumor therapy strategy could be comprised by intracellular antioxidants, especially GSH and thioredoxin (Trx). They are both cofactors of Gpx4, the enzyme catalyzing the production of lipid peroxides to relieve oxidative stress, which drives the acquired ferroptosis resistance in tumors. Herein, the NADPH-consuming micelles are specially designed, which could collaborate with the ROS generating photodynamics therapy (PDT) by depleting intracellular GSH and Trx under hypoxia condition, resulting in ruined redox homeostasis and the final cascade amplified ferroptosis. The tailored micelle was briefly prepared by conjugating hypoxia-sensitive segment p-nitrobenzyl chloroformate (PNZ-Cl) to the hydrophilic chitosan (CS), the resulting micelle was further modified with photosensitizer Ce6 via PEG linkage. When receiving laser irradiation, the photosensitizer would generate ROS and consume oxygen in the meanwhile. The resulting anabatic hypoxia in turns promote the NTR-catalyzed electron-accepting response of micelles, with evidently enhanced NADPH consumption and ultimately ruined redox homeostasis, contributing to cascade amplified ferroptosis with robust ROS. Most importantly, the accompanied immunogenic cell death (ICD) and releasing danger-associated molecular patterns (DAMPs) could boost dendritic cells (DCs) maturation and the subsequent T-cell-mediated profound immune response. Collectively, the work excavates the other biochemical reaction during the hypoxia-sensitive process of C–N–Ce6 by diminishing intracellular GSH and Trx, providing a candidate of ferroptosis inducers against solid tumors.

## 1. Introduction

Ferroptosis is known as a programmed cell death with altered iron and redox homeostasis, contributing to impaired cell structure and integrity [1]. Ferrous ion, PE-AA-OOH and defective Gpx4 are generally believed to be three major hallmarks of ferroptosis [2]. In the recent years, a growing number of researches concerning ferroptosis in treating cancers. However, persister cells or cancer stem cells are present across a wide range of tumor types and are resistant to chemotherapy or some other therapies, leading to disease relapse. According to previous reports, the survival of above cells was closely related with Gpx4 level [3,4], which gives rise to strategy in targeting Gpx4 to handle drug resistance and impair tumor relapse.

GSH and thioredoxin (Trx) are believed to be two antioxidant pathways generally work together to facilitate tumor progression [5,6]. Therefore, dual inhibition of these two systems might promise synergistic effects in killing cancer cells. GSH is reported to protect cells from ferroptosis via Gpx4/GSH axis, while Trx could also donate electron to Gpx4. As presented in Scheme 1, the recycle of GSH and Trx antioxidant systems largely depend on the participation of NADPH, which donates electrons and aids the reduction of oxidized glutathione (GSSG) to GSH by glutathione reductase (GR) and oxidized thioredoxin to Trx by thioredoxin reductase (TrxR). Usually, NADPH is depleted during ferroptosis, which may serve as exclusive predictor for ferroptosis susceptibility.

Hypoxia condition in solid tumor favors the overexpression of oxidoreductase nitroreductase (NTR) and reducing agent NAD(P)H [7].

* Corresponding author.
*E-mail address:* hufq@zju.edu.cn (F. Hu).
[1] These authors contributed equally to this work.

https://doi.org/10.1016/j.mtbio.2022.100532
Received 27 October 2022; Received in revised form 13 December 2022; Accepted 26 December 2022
Available online 5 January 2023

The bio-reductive hypoxia tumor environment expedites the development of hypoxia-activated nanoparticles, which could be catalyzed by the overexpressed NTR and consuming the NADPH in the meanwhile. Thus, it is hypothesized that the hypoxia-activated nanoparticles containing nitrobenzene may response to NTR and deplete NADPH in the meanwhile, which would later modulate both Gpx4/GSH and Gpx4/Trx axes to settle the resistance problem mediated by Gpx4 in ferroptosis antitumor therapy mentioned above. Generally, the reducing agents, including GSH and Trx $(SH)_2$ would decline when NADPH depletion occurs, which ulteriorly impair the activity of Gpx4. The strategy utilizing the natural feature of nano drug delivery systems is much favored here.

ROS could act as the center for inducing ferroptosis, which would disturb the redox homeostasis [8]. Photodynamic therapy (PDT) would induce robust ROS generation under laser irradiation, which makes it appropriate candidate in inducing ferroptosis when combined with GSH depletion [9]. Besides, the immunogenic cell death (ICD) could be triggered by PDT, which in turns activates the T-cell adaptive immune response and constructs long-term immunological memory [10,11]. Hence, here we propose the combinational strategy of coupling ROS-generation and NADPH-depletion by designing drug-free photosensitizer conjugated electron-accepting micelles as displayed in Scheme 1. The tailored micelle was briefly prepared by conjugating hypoxia-sensitive segment p-nitrobenzyl chloroformate (PNZ-Cl) to the hydrophilic chitosan (CS), the resulting micelle was further modified with photosensitizer Ce6 via PEG linkage. When receiving laser irradiation, the photosensitizer would generate ROS and consume oxygen in the meanwhile. The resulting anabatic hypoxia in turns promotes the NTR-catalyzed electron-accepting response of micelles, with evidently enhanced NADPH consumption and ultimately ruined redox homeostasis, amplifying ferroptosis with robust ROS.

## 2. Experimental section

### 2.1. Materials

Chitosan (CS, Mw = 5 kDa) of low molecular weight was obtained by enzymatic degradation of chitosan (95% deacetylated, Mw = 240 kDa, supplied by Yuhuan Marine Biochemistry Co., Ltd, Zhejiang, China). P-nitrobenzyl chloroformate (PNZ-Cl), 5,5′-Dithio bis-(2-nitrobenzoic acid)(DTNB) and Coenzyme II reduced tetrasodium salt (NADPH) were purchased from Aladdin. 6-Aminocaproic acid, 1,3-

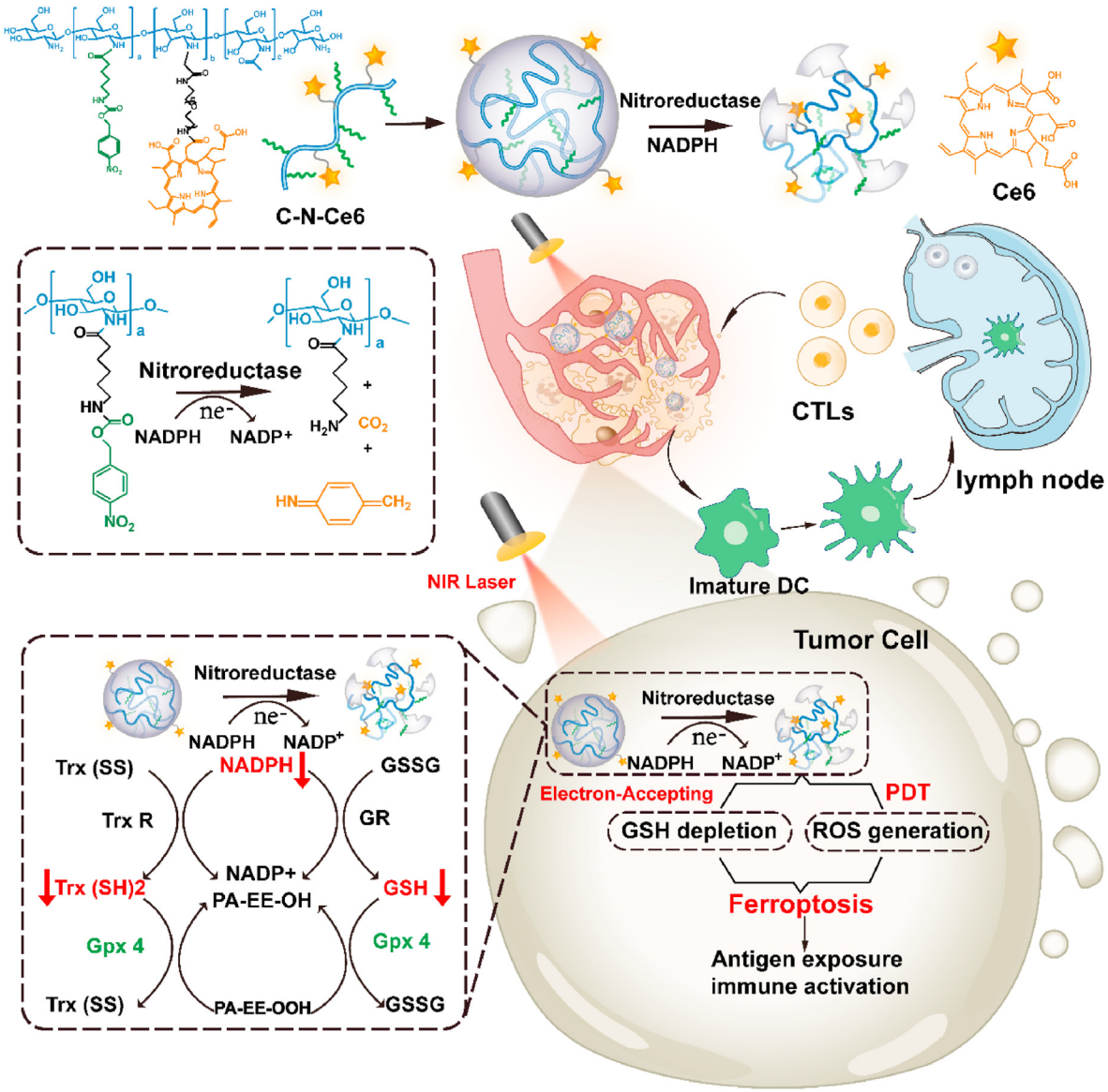


**Scheme 1.** Combinational strategy of coupling ROS-generation and NADPH-depletion by designing drug-free photosensitizer conjugated electron-accepting micelles.

Diphenylisobenzofuran (DPBF), NH2-PEG2000-NH2, 1-ethyl-3-(3-dimethyl-aminopropyl) carbodiimide (EDC), and NTR were obtained from Sigma-Aldrich Inc. Triethylamine (TEA), N,N-dimethylformamide (DMF), dimethyl sulfoxide (DMSO), ethyl acetate, ethanol, and dichloromethane (DCM) were purchased from Sinopharm Chemical Reagent Co., Ltd, China. DiO and DiI were bought from Dalian Meilun Biotech Co., Ltd. Chlorin e6(Ce6) was obtained from Shanghai Yuanye Corp. 2,4,6-trinitrobenzene sulfonic acid (TNBS) was purchased from Sigma (St. Louis, MO, USA), glutathione (GSH) assay kit (Nanjing Jiancheng Bioengineering Institute, China), Fluorescein diacetate (FDA) and propidium iodide (PI) were obtained from Thermo Fisher Scientific (Waltham, MA, USA). Mounting Medium, antifading was obtained from Beijing Solarbio Science & Technology Co., Ltd.

### 2.2. Synthesis and characterization of electron-accepting micelles C–N and C–N–Ce6

C–N–Ce6 was synthesized in the following two steps.

Firstly, we prepared C–N based on the method previously reported in our lab [12].Briefly, 6-Aminocaproic acid reacted with 4-Nitrobenzyl chloroformate to generate intermediate 1. Subsequently, under the activation of EDC, the carboxyl group on the intermediate 1 reacted with the amino group of chitosan to obtain the reaction solution. The reaction solution was dialyzed against DI water using a dialysis membrane (MWCO = 3.5 *k*Da) for 48 h. C–N solid powder was collected by freeze-drying.

Secondly, we used $NH_2$-$PEG_{2000}$-$NH_2$ to connect Ce6 and C–N to prepare C–N–Ce6. In a dark environment, Ce6 (30 mg) , EDC (70 mg) and NHS (52 mg) were dissolved in DMF and stirred for 2 h at 25 °C. $NH_2$-$PEG_{2000}$-$NH_2$ (120 mg) was added into the reaction solution and stirred for 8 h. Then DSC (16 mg) was added and continued stirring for 16 h. The preparation of reaction solution 1 was completed. C–N (150 mg) dissolved in DI water was added into reaction solution 1. After stirring for 24 h, the final product was dialyzed against DI water using a dialysis membrane (MWCO = 3.5 *k*Da) for 48 h. C–N–Ce6 solid powder was gained by lyophilization.

The chemical structure of C–N and C–N–Ce6 were analyzed by $^1$HNMR spectroscopy. A particle size and potential analyzer was used to detect the particle size and ζ potential of each compound. The corresponding evolution in morphology and size of each compound were observed by TEM imaging and DLS. A pyrene fluorescent probe was used to determine the critical micelle concentrations (CMCs) of C–N and C–N–Ce6. The degrees of amino substitution of C–N and C–N–Ce6 were determined by the 2,4,6-trinitrobenzene sulfonic acid (TNBS) method to prove the conjugation of Ce6.

### 2.3. Evaluation of micelle collapse in vitro in mimicked hypoxia conditions

A particle size analyzer was used to detect the collapse of nanoparticles in vitro. Firstly, the prepared micelles were suspended in PBS solution (pH 7.4) with different concentrations of NTR and NADPH (0 μg $mL^{-1}$ NTR+0 μmol $L^{-1}$ NADPH or 10 μg $mL^{-1}$ NTR+100 μmol $L^{-1}$ NADPH), which was adopted to simulate the in vitro hypoxia environment. The changes of particle size were monitored as time went by. For the purpose of observing the morphologic change, the samples were further subjected to TEM test.

In vitro FRET test was done under mimicked hypoxia conditions. The FRET pair, DiO and DiI, was physically coencapsulated in C–N–Ce6 to prepare C–N–Ce6/DiO-DiI. the prepared micelles were suspended in PBS solution (pH 7.4) with different concentrations of NTR and NADPH ((0 μg $mL^{-1}$ NTR+0 μmol $L^{-1}$ NADPH or 10 μg $mL^{-1}$ NTR+100 μmol $L^{-1}$ NADPH), which was adopted to simulate the in vitro hypoxia environment. All samples were excited at 484 nm with 501 nm and 565 nm emission channel. The FRET efficiency was calculated as the fluorescence intensity at 565 nm being divided by the sum of fluorescence intensity at 565 nm and 501 nm.

FRET assay was also done to monitor the depolymerization of the prepared C–N–Ce6 in cells. 4T1 cells were seeded in 24-well plates overnight and then treated with 100 μM $CoCl_2$ for 8 h, where the $CoCl_2$ acted as the agent to mimic hypoxia. After that, C–N–Ce6/DiO-DiI was added to hypoxia and normoxia groups for 2 h, then the cell culture media was refreshed with new DMEM media, the cells were further cultured under normoxia or hypoxia for determined time (0, 2 and 4 h). All samples were excited at 488 nm with two separate emission ranges (500–550 nm and 575–620 nm). The FRET ratio was defined as the fluorescence intensity at 575–620 nm, being divided by the sum of the intensities at 500–550 nm and 575–620 nm, and plotted against time (n = 3).

### 2.4. Cell and animals

4T1 cells (a mouse breast cancer cell line) were cultured in DMEM, which was purchased from the Cell Bank of Shanghai Institute of Biochemistry and Cell Biology, Chinese Academy of Sciences (Shanghai, China), supplemented with 10% fetal calf serum (v/v), 10000 U $mL^{-1}$ streptomycin and 10000 U $mL^{-1}$ penicillin at 37 °C in a humidified incubator with 5% $CO_2$. All studies were approved by the Zhejiang University Laboratory Animal Welfare Ethics Review Committee and were conducted in accordance with national regulations and protocols.

### 2.5. Cellular uptake of micelles

4T1 cells ($5 \times 10^5$ cells per mL) were seeded in 6-well plates and cultured at 37 °C overnight. After that, the cells were treated with free Ce6 and C–N–Ce6 (Ce6 concentration = 0.5 μg $mL^{-1}$). After incubating for appointed time, the cells were collected and washed with PBS, which were further subjected to flow cytometry assay to evaluate the cellular uptake of micelles at different times.

### 2.6. Intracellular redox biomarker analysis

4T1 cells were seeded in 6-well plates with the density at $5 \times 10^5$ cells per well, followed with the addition of $CoCl_2$ to stimulate the hypoxia environment overnight. Afterwards, the cells were incubated with PBS, C–N and C–N–Ce6 for 1 h with PBS group as the control group, the concentration of C–N and C–N–Ce6 was 100 μg $mL^{-1}$. Subsequently, the cells were collected and subjected to $NADP^+$/NADPH assay by the commercial $NADP^+$/NADPH assay Kit (Beyotime Biotechnology, China). The total proteins were quantified by the commercial BCA protein assay kit (Beyotime Biotechnology, China). Similarly, The GSH quantification were utilizing the commercial GSH assay kit (Jiancheng bioengineering institute, China). In the meanwhile, the levels of total thiols and reduced Trx were evaluated by DTNB titration method.

### 2.7. In vitro and intracellular ROS evaluation

The ability for singlet oxygen generation was studied using the probe DPBF due to the ability of singlet oxygen in decreasing the absorbance of DPBF. Briefly, 0.5 mg $mL^{-1}$ DPBF was mixed with $H_2O$, C–N, physical mixture of C–N and Ce6, free Ce6 and C–N–Ce6 respectively (Ce6 concentration = 0.25 μg $mL^{-1}$, C–N concentration = 3.125 μg $mL^{-1}$). All samples were treated with laser irradiation (660 nm, 0.8 W/$cm^2$) for 2 min. The characterization was performed at 410 nm wavelength depending on a UV–vis spectrophotometer.

ROS levels were detected by the ROS probe DCFH-DA according to previous report. Briefly, $5 \times 10^4$ cells per well were seeded into each well of a 24-well plate at 37 °C overnight. Afterwards, cells were treated with PBS, C–N, free Ce6 and C–N–Ce6 (Ce6 concentration = 0.2 μg $mL^{-1}$, C–N concentration = 2.5 μg $mL^{-1}$), after another 12 h incubation, the culture media was replaced with new DMEM. Cells were treated with or without laser irradiation (660 nm, 0.8 W/$cm^2$, 3 min). After that, the medium was removed, the cells were washed with PBS for three times. The cells were

then incubated with 10 μM DCFH-DA dye for around 30 min. Afterwards, the cells were stained with Hoechst and observed by CLSM.

### 2.8. Ferroptosis and Gpx4 analysis in vitro

The intracellular sites of lipid hdroperoxide accumulation were detected by the ferroptosis probe BODIPY 581/591C11 according to previous report. Briefly, $5 \times 10^4$ cells per well were seeded into each well of a 24-well plate at 37 °C overnight. Afterwards, cells were treated with PBS, C–N, free Ce6 and C–N–Ce6 (Ce6 concentration = 0.2 μg $mL^{-1}$, C–N concentration = 2.5 μg $mL^{-1}$), after another 12 h incubation, the culture media was replaced with new DMEM. Cells were treated with or without laser irradiation (660 nm, 0.8 W/$cm^2$, 3 min). After 6 h, the medium was removed, the cells were washed with PBS for three times. The cells were then incubated with 10 μM BODIPY 581/591C11 dye for around 30 min. Afterwards, the cells were stained with Hoechst and observed by CLSM. Similarly, the cells under same treatment was stained with JC-1 dye to evaluate mitochondria potential.

4T1 cells ($5 \times 10^5$ cells per mL) were seeded in 6-well plates and treated with 100 μM $CoCl_2$ for 8 h, after that PBS, C–N, Ce6 and C–N–Ce6 (C–N/C–N–Ce6 = 10 μg $mL^{-1}$, Ce6 = 0.8 μg $mL^{-1}$) were added and further incubated for 8 h under hypoxia environment. Then cells of different groups were collected for WB test to evaluate the expression of Gpx4. Similarly, 4T1 cells ($5 \times 10^5$ cells per mL) were seeded in 6-well plates overnight. Afterwards, the cells were washed with PBS for three times, followed by the addition of fresh medium and PBS, C–N, Ce6 and C–N–Ce6 (C–N/C–N–Ce6 = 10 μg $mL^{-1}$, Ce6 = 0.8 μg $mL^{-1}$) separately. After incubation for 12 h, the culture media was changed for fresh medium and treated with laser irradiation (660 nm, 0.8 W/$cm^2$, 3 min). After another incubation for 8 h. The cells were collected for WB assay to measure Gpx4 expression.

### 2.9. In vitro cytotoxicity analysis

MTT assays were used to evaluate in vitro cytotoxicity of Ce6 and C–N–Ce6 with and without laser irradiation (660 nm, 0.8 W/$cm^2$, 3 min). Briefly, $2 \times 10^3$ cells per well were seeded into each well of a 96-well plate at 37 °C overnight. Ce6 and C–N–Ce6 were added in replicates of six at the designed concentrations of 0, 0.25, 0.5, 1, 1.5 μg $mL^{-1}$ and incubated for 12 h, then the cultured media was abandoned and replaced with fresh DMEM media. The cells were treated with/without laser irradiation (660 nm, 0.8 W/$cm^2$, 3 min). After another 24 h of incubation., each well was added with 20 μL of MTT solution and incubated for 4 h. Finally, the medium was removed and added with 200 μL DMSO. The absorbance was measured by ultraviolet spectrophotometer at 570 nm to calculate the cell viability. Similarly, in order to verify the ferroptosis mechanism of C–N–Ce6, the inhibitor of ferroptosis GSH and vitamine E (VE) were adopted.

### 2.10. In vivo distribution assay

A 4T1 breast tumor xenograft model was established to monitor the in vivo distribution of the nanoparticles. The distribution assay was done when the volume of the tumor reached approximately 100 $mm^3$. Free Ce6, C–N–Ce6 were intravenously administrated to the mice. The fluorescence of Ce6 itself could be photographed to monitor the distribution of micelles in mice. The mice were imaged with a Maestro in vivo imaging system (CRI Inc., Woburn, MA) at predesigned time. After 24 h, mice were sacrificed, the fluorescent signals from Ce6 in tumor sessions and major organs were imaged under same parameters. In the meanwhile, all tumor tissues were subjected to frozen sectioning to acquire microscopic sections, which were later stained with DAPI and visualized by confocal microscopy to evaluate the distribution of micelles in deep tumor region.

### 2.11. In vivo antitumor evaluation

A 4T1 breast tumor xenograft model was established to evaluate the antitumor efficacy of the nanoparticles. All tumor-bearing mice were randomly divided into five groups: 1) PBS; 2) C–N; 3) Ce6; 4) C–N + Ce6; 5) C–N–Ce6. When the tumor reached about 100 $mm^3$, the mice were intravenously injected with PBS, C–N, Ce6, C–N + Ce6 and C–N–Ce6 every two days for 6 times. Besides, all of mice were treated with laser irradiation (660 nm, 0.8 W/$cm^2$, 5 min). In the meanwhile, the tumor size and body weights were recorded every two days to monitor antitumor efficiency and safety. On the 15th day, the mice were sacrificed. The excised major organs and tumor massed were collected and fixed in 4% paraformaldehyde solution. HE staining and Tunel staining were done on major organs and tumor masses. The sections were observed via the optical microscope.

In order to evaluate the immune activation activity of prepared nanoparticles. Isolated tumors were ground to obtain single-cell suspensions. After blood cell clearance, cells were preincubated with 1% BSA solutions and then labelled with antibodies (APC-labelled CD206, PE-labelled F4/80, PE labelled Gr-1, PerCP-cy5.5 labelled CD11b, APC labelled CD3, FITC labelled CD4, PE labelled CD8, PE labelled CD80, APC-cy7 labelled CD86 and FITC labelled CD11c) for flow cytometry analysis.

### 2.12. Statistical analysis

All data are presented as the mean ± standard deviation. Differences were analyzed by two-tailed Student's t-test and one/two-way ANOVA. A p-value $<0.05$ was considered statistically significant.

## 3. Results and discussion

### 3.1. Synthesis and characteristics of C–N and C–N–Ce6

Briefly, C–N was simply prepared according to previous report in our lab [12]. Ulteriorly, C–N–Ce6 was prepared by grafting Ce6 on chitosan skeleton via PEG chain as displayed in Fig. 1A. For the sake of verifying the successful conjugation of Ce6 onto C–N, the chemical structures of chitosan, PNZ-Cl, 6-amino-caproic acid, C–N, Ce6, PEG and C–N–Ce6 were analyzed by $^1$H NMR (Fig. 1B&C). Similarly, the peaks located around 1.2–1.4 ppm and 3–4 ppm belonged to $–CH_2–$ of 6-amino-caproic and alkyl ether of chitosan in C–N, respectively. Simultaneously, the peaks at 7.5–8.0 was attributed to the nitrobenzene of PNZ-Cl, further verifying the successful synthesis of C–N. In the meanwhile, the peak at around 3.5 ppm in PEG was appeared in C–N–Ce6, which was supposed to be the $–CH_2–$ in PEG chain. Apart from that, the –COOH– at 12.5 ppm in Ce6 spectrum disappeared in C–N–Ce6, while the peak in 2.5 ppm was reserved instead, indicating the successful conjugation of Ce6 onto C–N via PEG chain. In the meanwhile, GPC was adopted to demonstrate the coupling of PEG-Ce6 to CS as illustrated in Fig. S1. The retention time of C–N–Ce6 was decreased when compared with CS, which changed from 27.084 to 24.063, suggesting larger molecular weight of C–N–Ce6. UV–vis spectra were utilized here to evaluate the synthesis as Fig. 1D. Obviously, the final preparation C–N–Ce6 was equipped with characteristic peaks in Ce6 and C–N. Specially, compared with C–N, peaks at around 400 and 630 nm was newly appeared in C–N–Ce6 and the UV absorption in 240–280 nm was slightly increased. Apart from that, FTIR spectrum was done here as displayed in Fig. S2. New peak in 2884 $nm^{-1}$ of C–N–Ce6 belongs to the stretching vibration of C–H bonds in PEG, which was also appeared in PEG at 2887 $nm^{-1}$. Similarly, the peak at 1111 $nm^{-1}$ in C–N–Ce6 was attributed to the stretching vibration of C–O bonds in PEG at 1113 $nm^{-1}$, verifying the successful incorporation of PEG. In the meanwhile, the peak of N–H bond in Ce6 at 1608 $nm^{-1}$ could also observed in C–N–Ce6, which located at 1561 $nm^{-1}$, indicating the successful conjugation of Ce6. According to previous report, the degree of amino substitution (the substitution degree of the active amino groups on

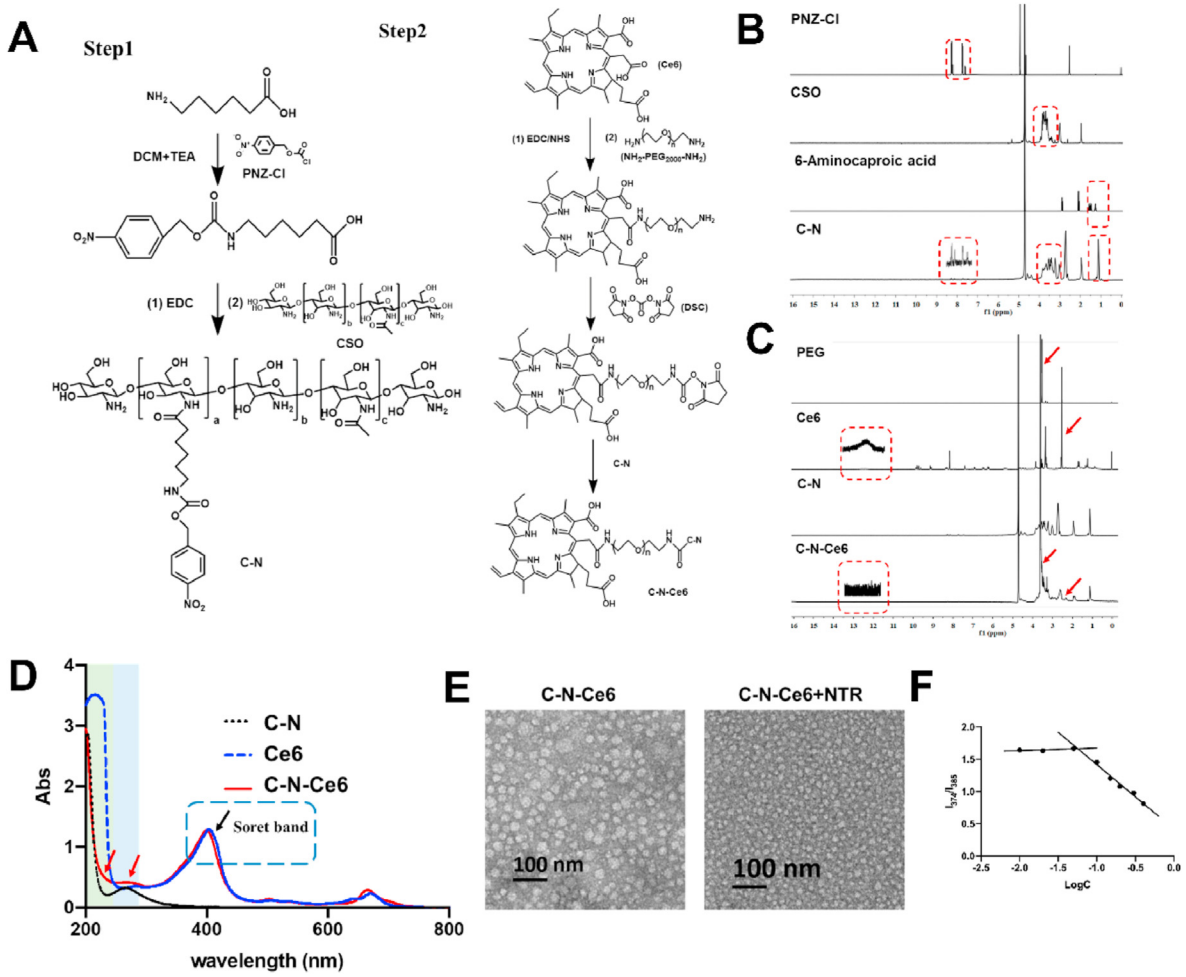


**Fig. 1.** Synthesis and characteristics of C–N and C–N–Ce6. (A) Synthesis route of C–N and C–N–Ce6. (B) 1H NMR spectrum of PNZ-Cl, CSO, 6-Aminocaproic acid and C–N. (C) 1H NMR spectrum of PEG, Ce6, C–N and C–N–Ce6. (D) UV–Vis results of C–N, Ce6 and C–N–Ce6. (E) TEM results of C–N–Ce6 and C–N–Ce6 +NTR. Scale bar: 100 nm. (F) The I1/I3 ratio of fluorescence intensity of pyrene as a function of the logarithmic concentration (Log C) of C–N–Ce6.

the chitosan chain) of C–N and C–N–Ce6 was measured by 2,4,6-trinitrobenzene sulfonic acid (TNBS) [13], which was measured to be 10.48% and 12.06% respectively. It was not hard to find that the degree of amino substitution was increased after the conjugation of Ce6, reflecting the successful grafting of Ce6 from the side.

Owning to the amphiphilic structure of C–N–Ce6, which can self-assemble in water to form micelles. The particle size and distribution of C–N and C–N–Ce6 were determined by DLS as shown in Table 1. The particles sizes of C–N and C–N–Ce6 were 132.6 ± 3.8 and 172.7 ± 4.9 respectively, which was slightly increased of C–N–Ce6 when grafted with Ce6. The zeta-potential of C–N and C–N–Ce6 was 31.0 ± 1.3 and 32.4 ± 1.0 mV with neglectable change. Furthermore, transmission electron microscopy (TEM) was adopted to observe the morphology of C–N–Ce6. As illustrated in Fig. 1E, C–N–Ce6 showed spheroid-like properties and mono-dispersity. The critical micelle concentration (CMC) value of C–N–Ce6 was detected by pyrene according to previous report [13], which was measured to be 56.69 μg/mL as displayed in Fig. 1F, indicating the favorable self-assembling ability of C–N–Ce6. The stability of C–N–Ce6 was monitored under PBS solution with 10% fetal bovine serum (FBS, v/v) to mimic physiological environment. It could be observed in Fig. S3 that the particle size was barely changed during 48 h, which was measured to be around 200 nm, verifying the stability of C–N–Ce6 under physiological environment.

**Table 1**
Characteristic of micelles.

| Nanoparticles | Size/nm | PDI | Zeta/mV |
|---|---|---|---|
| C–N | 132.6 ± 3.8 | 0.280 ± 0.008 | 31.0 ± 1.3 |
| C–N–Ce6 | 172.7 ± 4.9 | 0.268 ± 0.011 | 32.4 ± 1.0 |

### 3.2. *Hypoxia-responsive properties of C–N–Ce6 micelles accompanied with electron acceptance*

It is commonly recognized that hypoxia is a typical hallmark of cancer according to previous report [14]. Herein, NTR, an active component in hypoxia tumor environment, is adopted here to stimulate in vitro hypoxia environment to learn the hypoxia-responsive behavior of C–N–Ce6. Upon hypoxia environment, the nitrobenzene structure in C–N–Ce6 would be reduced to amino groups and degraded, resulting in the depolymerization of the micelles. As usual, the dynamic changes of particle size were monitored by DLS at determined time as shown in Fig. 2A. The particle sizes of C–N–Ce6 under simulative hypoxia environment presented a rapid decrease at the beginning 10 min, which went through a sharp decrease at 40 min, it was measured below 1 nm. At 60 min after the incubation, the particle size could not be detected, indicating the hypoxia behavior of C–N–Ce6. TEM results were also photographed to verify the hypoxia-sensitive behavior. Obviously, the particles dramatically decreased after the addition of NTR enzyme, which was consist with the DLS results.

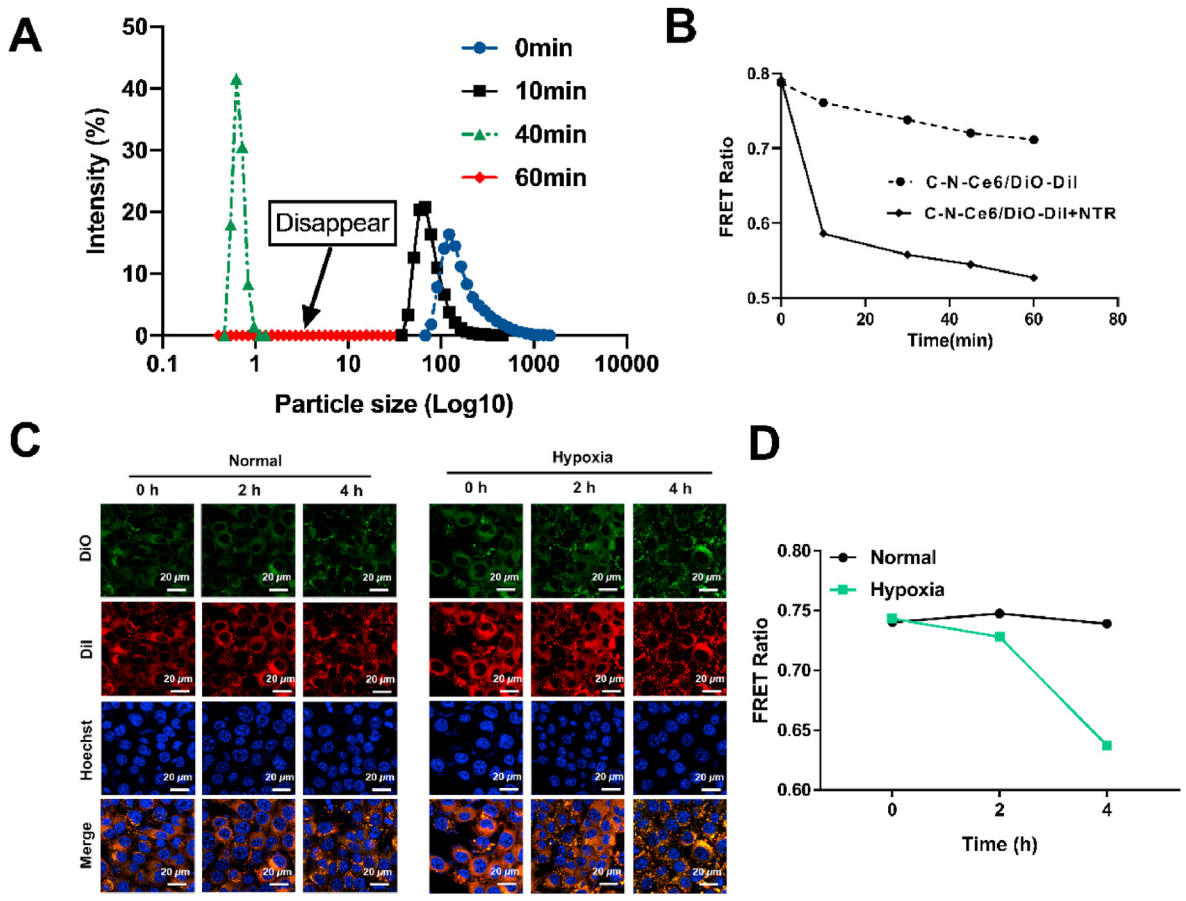


**Fig. 2.** Hypoxia-responsive properties of C–N–Ce6 micelles. (A) Particle size changes after NTR incubation at appointed time of 0, 10, 40 and 60 min. (B) Kinetic FRET ratio of C–N–Ce6/DiO-DiI with or without NTR incubation as time went by. (C) FRET analysis of hypoxia-responsive micelles (C–N–Ce6/DiO-DiI). Scale bar: 20 μm. (D) The corresponding quantification of the FRET ratio.

Apart from TEM and DLS, FRET assay was done in vitro to evaluate the responsive property. Here, DiO/DiI FRET pair was employed according to previous reports [15,16]. All samples were excited at 484 nm with two corresponding emission channels (501 nm and 565 nm). The FRET ratio was defined as the fluorescence intensity at 565 nm, being divided by the sum of the fluorescence intensity at 501 nm and 565 nm, and plotted against time. As shown in Fig. 2B, we could infer that the FRET ratio evidently decreased when the NTR enzyme was added compared with control group, which reached around 0.5 at 1 h past the incubation, indicating the depolymerization of the micelles upon the stimulated hypoxia environment, further revealing the hypoxia-responsive characteristic of C–N–Ce6.

### 3.3. Evaluation of the intracellular stimuli-responsive degradation of the nanoparticles

FRET assay was also displayed in cells to evaluate the hypoxia-responsive behavior. Similarly, FRET pair DiO/DiI was also employed here. According to the results in Fig. 2C and semi-quantitative results in Fig. 2D, the FRET analysis of cargo release in C–N–Ce6 treated cells showed a rapid decline of FRET ratio against time under hypoxia environment, revealing the separation of FRET pair on account of the depolymerization of C–N–Ce6 micelles, while it showed negligible change in control group as expected, further verifying the hypoxia-sensitive feature of C–N–Ce6 in intracellular level.

### 3.4. Micelles-induced imbalance of redox homeostasis

It was mentioned above that the C–N–Ce6 would response to hypoxia environment and consume NAPDH in the meanwhile, which later influence the content of GSH and Trx, resulting in the imbalance of redox homeostasis as illustrated in Fig. 3A. The $NADP^+$/NADPH was specially selected as the index to assess the ability of C–N–Ce6 in depleting NADPH under hypoxia situation as Fig. 3B. Under normoxic environment, the C–N–Ce6 didn't exhibit any impact on $NADP^+$/NADPH ratio. On the contrast, $NADP^+$/NADPH ratio was dramatically increased after the treatment of C–N–Ce6 under hypoxia environment, verifying the NADPH depletion effect of C–N–Ce6 itself. In the meanwhile, the intracellular GSH, total thiol and Trx levels were also assayed. Similarly, the levels of GSH, total thiol and Trx had not been altered in normoxic conditions, while they were reduced upon the addition of C–N–Ce6 under hypoxia condition as displayed in Fig. 3C and D and Fig. 3E. Ulteriorly, the activity of Gpx4 was evaluated due to its special position in ferroptosis as displayed in Fig. 3F. C–N–Ce6 induced the inactivation of Gpx4 under hypoxia, while the activity of Gpx4 was not impaired under normoxic environment.

### 3.5. In vitro measurements of cytotoxicity and uptake of C–N–Ce6

Firstly, the cytotoxicity of blank micelle C–N at determined concentrations was also evaluated. C–N didn't show obvious cytotoxicity on 4T1 cells with or without laser irradiation shown in Fig. 4A, verifying the

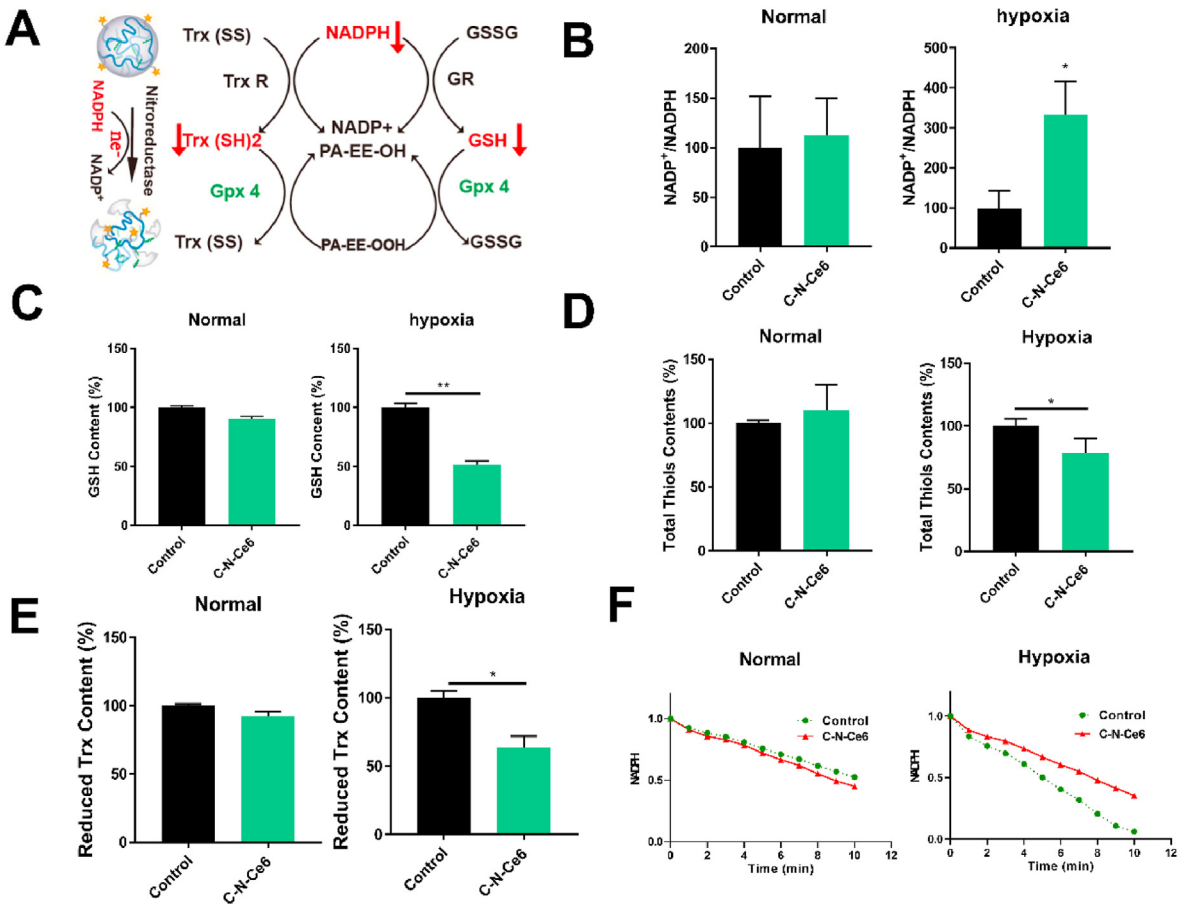


**Fig. 3.** Micelles-induced imbalance of redox homeostasis. (A) Illustration of the mechanism C–N–Ce6 -induced imbalance of redox homeostasis. Relative intracellular NADP+/NADPH ratio(B), GSH(C), total thiols (D) and thioredoxin levels (E) under normoxia or hypoxia. (F) Activity of Gpx4 upon treatment by C–N–Ce6 under normoxia or hypoxia. *$p < 0.05$, $n = 3$.

biocompatibility of the prepared C–N micelle. Subsequently, the relevant cytotoxicity of free Ce6 and C–N–Ce6 on 4T1 cells was assessed by MTT assay as shown in Fig. 4B. The introduce of Ce6 didn't show apparent cytotoxicity to C–N. In contrast, the cell viability was even higher in C–N–Ce6 group than that in Ce6 group when the Ce6 concentration was at 1.5 μg $mL^{-1}$ without laser irradiation. In the meanwhile, the cells receiving Ce6 and C–N–Ce6 treatment were subjected to 660 nm NIR laser irradiation, it was suggested that the C–N–Ce6 presented better inhibitory effect on cell viability than free Ce6 when the concentration of Ce6 exceeded 0.5 μg/mL, which may occur as a result of the enhanced cellular uptake of C–N–Ce6 and the amplified ferroptosis. We further carried cytotoxicity experiments under hypoxia to evaluate the cytotoxic effects of C–N and C–N–Ce6 under hypoxic environment. As shown in Fig. S4, C–N and C–N–Ce6 barely impacted cell viability under normoxic environment, while in hypoxic condition, C–N and C–N–Ce6 displayed cytotoxicity when the concentration was 12.5 μg $ml^{-1}$ (the concentration of Ce6 was 0.5 μg $mL^{-1}$). The cell viability was only around 80% when the concentration of C–N and C–N–Ce6 was 100 μg $mL^{-1}$ (the concentration of Ce6 was 4 μg $mL^{-1}$). It was not hard to find that the inhibitory of C–N or C–N–Ce6 on 4T1 cells was limited. Thus, the strategy of combing ROS-generator Ce6 and NADPH-consuming micelles was of great importance.

In vitro uptake of C–N–Ce6 at different times was monitored by flow cytometry to learn the intracellular behavior of C–N–Ce6. As shown in Fig. 4C and D, the fluorescence of Ce6 within cells was measured in both Ce6 and C–N–Ce6 groups. It was observed that the retention of Ce6 and C–N–Ce6 within cells was increased as a function of time, and the intracellular Ce6 fluorescence in C–N–Ce6 group was much higher than that in Ce6 group at all tested time intervals. We could conduct the conclusion that C–N–Ce6 could potentiate the cellular uptake of Ce6 molecules in 4T1 cells, which promises better therapeutic outcome.

Live and dead staining was done to verify the superiority of C–N–Ce6 in cytotoxicity, where green fluorescence signals represent the living cells and the dead cells produce red fluorescence [17]. Consistently, as displayed in Fig. 4E, the dead cells account for the main part with the treatment of C–N–Ce6 when under laser irradiation, while the dead cells were much less in Ce6 group. C–N treatment or cells in Ce6 and C–N–Ce6 groups without laser irradiation didn't show obvious impact on cell activity.

### 3.6. *Evaluation of the photodynamic performance of C–N–Ce6 nanoparticles*

At the beginning, the capability for ROS generation of C–N–Ce6 was learned under 660 nm NIR laser irradiation via the ROS probe DPBF [18]. The changes in UV–vis absorption spectra at 410 nm were recorded at determined times and shown in Fig. 5A. The blank micelle C–N didn't show any tendency in producing ROS, while C–N–Ce6 retained the photodynamic property of Ce6, demonstrating an excellent capability for rapid ROS generation under NIR laser irradiation. In the meanwhile, the ROS generation ability of C–N–Ce6 in cancer cells was also viewed with DCFH-DA as the probe. The green fluorescence intensity could directly reflect the ability for intracellular ROS production. As shown in Fig. 5B, free Ce6, blank C–N and the final preparation C–N–Ce6 didn't evidently increase the ROS production without NIR laser, while demonstrating a rapid ROS production when receiving NIR laser irradiation in Ce6 and

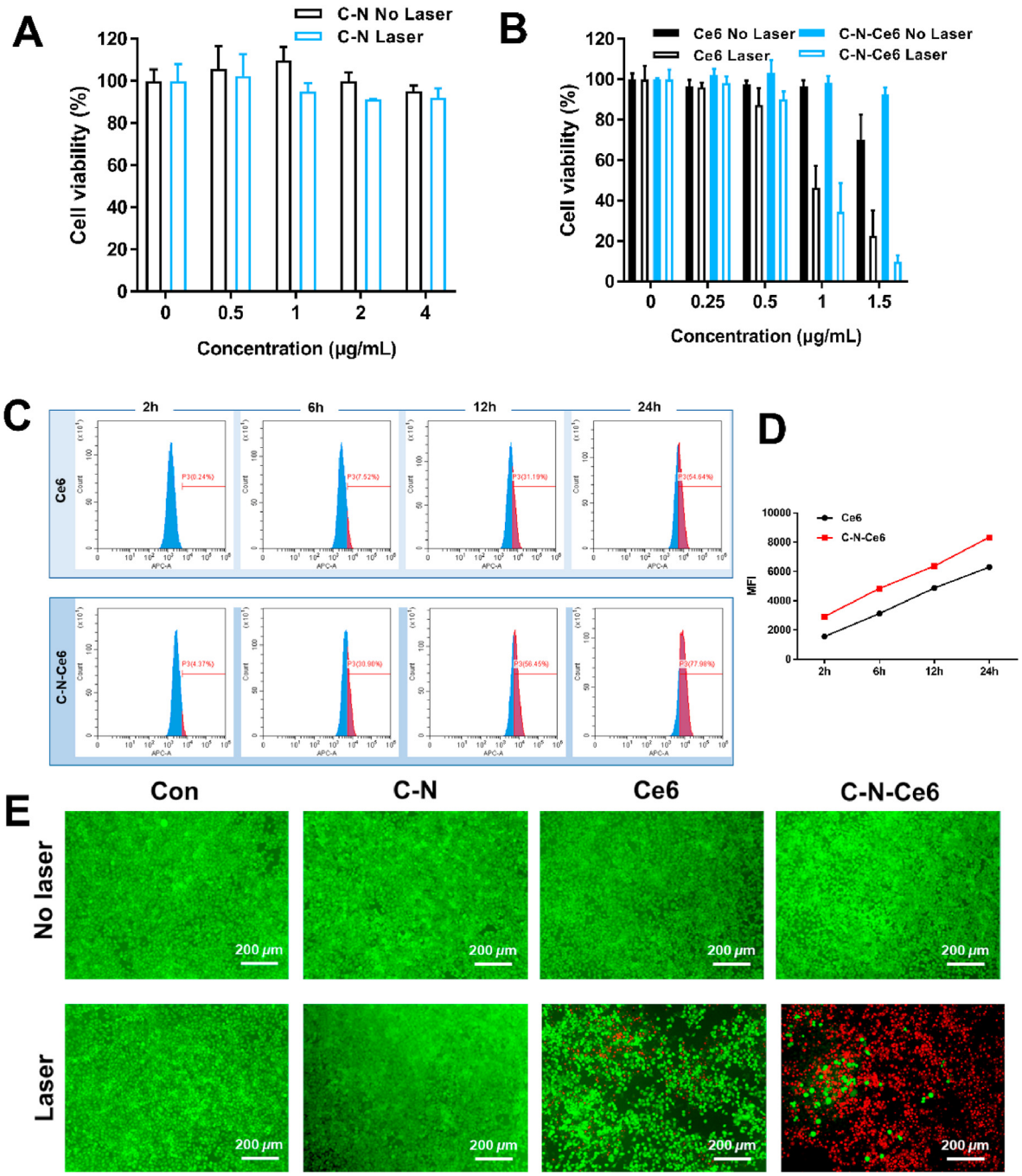


**Fig. 4.** In vitro measurements of cytotoxicity and uptake of C–N–Ce6. (A) The cytotoxicity of C–N in 4T1 cells with and without laser treatment. (B) The cytotoxicity of Ce6 and C–N–Ce6 in 4T1 cells with and without laser treatment. (C) The intracellular internalization of Ce6 and C–N–Ce6 as time went by measured by flow cytometry. (D) The mean fluorescence intensity of Ce6 and C–N–Ce6 in 4T1 cells in image D. (E) Live/Dead assays after PBS, C–N, Ce6 and C–N–Ce6 treatment with or without laser irradiation. The samples were observed using a fluorescence microscope. The living cells were denoted as green fluorescence signals while the dead cells produced red fluorescence. Scale bar: 200 μm. (For interpretation of the references to colour in this figure legend, the reader is referred to the Web version of this article.)

C–N–Ce6 group. Most noteworthy was the ROS production was the highest in C–N–Ce6, which may benefit from the combinational effect of ROS producing effect of Ce6 and the GSH-consuming function of C–N itself. Semi-quantitative results in Fig. 5C conducted the same conclusion, where the green fluorescence intensity in C–N–Ce6 group was 1.18-folds higher than that in Ce6 group when receiving laser irradiation.

### 3.7. Hypoxia-targeted enhancement of ferroptosis of C–N–Ce6

Oxygen-consuming photodynamic therapy would occur when cells treated with Ce6 were subjected to NIR laser irradiation. It was not hard to speculate that the hypoxia environment would be aggravated, which could be harnessed to exacerbate ferroptosis here. As the micelles C–N–Ce6 we designed here were sensitive to hypoxia environment, GSH-depletion would happen in the meanwhile, which could collaborate with ROS-generator Ce6 to amplify ferroptosis. Firstly, the oxygen-consuming behavior was investigated by hypoxia probe to detect the created hypoxia environment. As displayed in Fig. 5D, it could be seen that Ce6 and C–N–Ce6 groups receiving NIR laser irradiation dramatically consumed oxygen level and worsen hypoxia environment. 4T1 cells with same

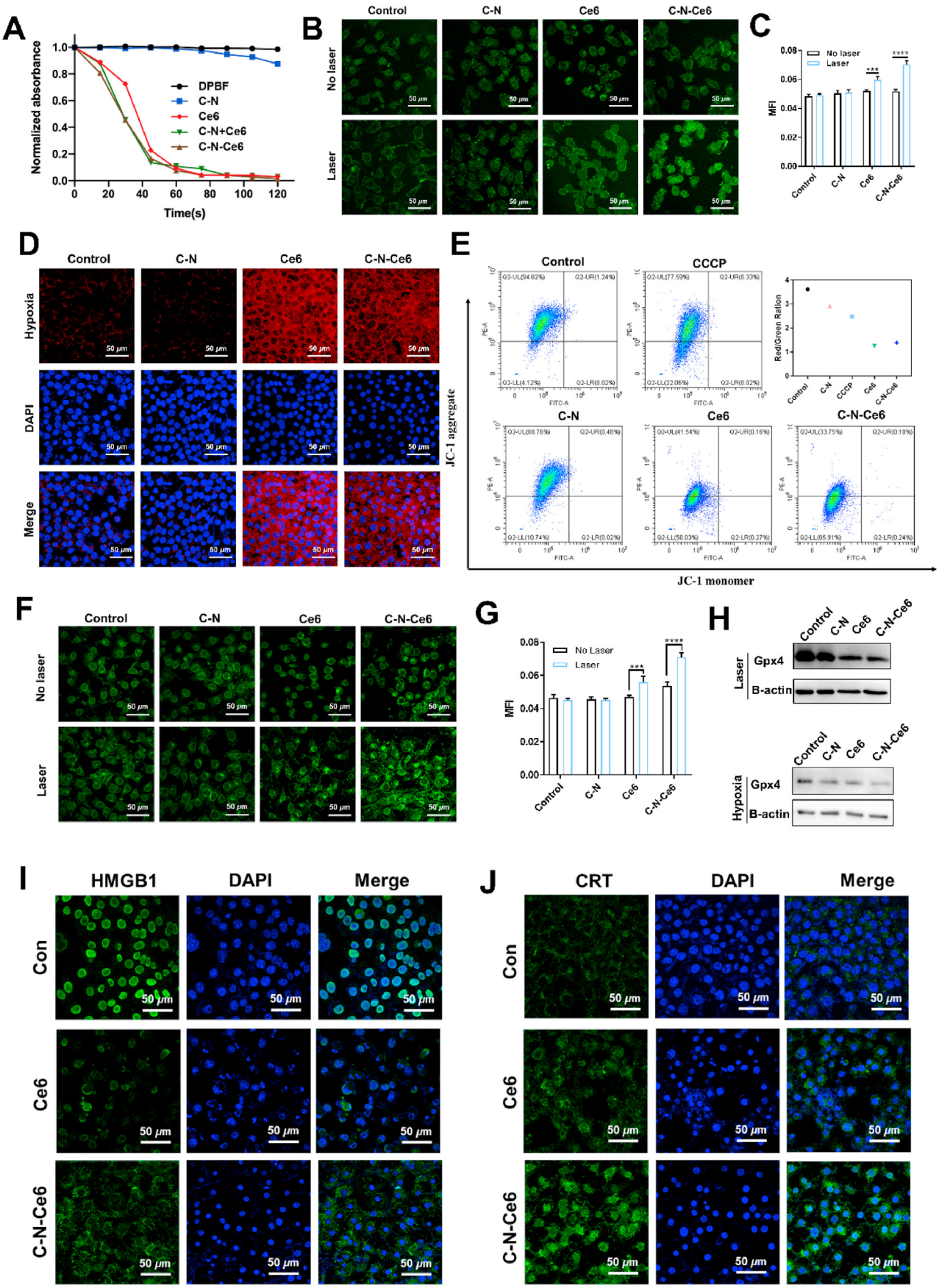


*(caption on next page)*

**Fig. 5.** Evaluation of the photodynamic and ferroptosis-inducing performance of C–N–Ce6 nanoparticles. (A) Normalized absorbance of DPBF at 410 nm in various samples (DPBF, C–N, Ce6, physical mixture of C–N and Ce6, and C–N–Ce6) during 2 min under laser irradiation. (B) ROS detection by ROS probe DCFH-DA in 4T1 cells with or without laser irradiation. The cells were treated with PBS, C–N, Ce6 and C–N–Ce6. Scale bar: 50 μm. (C) Semi-quantitative analysis of ROS fluorescent intensity in cells from image B. ***$p < 0.001$, ****$p < 0.0001$, $n = 3$. (D) Hypoxia level detected by Hypoxyprobe Red APC Kit. (E) Mitochondria membrane potential measured by JC-1 dye via flow cytometry. PE chancel represent JC-1 aggregate, FITC channel represent JC-1 monomer. (F) Fluorescent imaging of lipid peroxides in 4T1 cells with or without laser irradiation. The cells were treated with PBS, C–N, Ce6 and C–N–Ce6. Scale bar: 50 μm. (G) Semi-quantitative analysis of C11-BODIPY fluorescent intensity in cells from image B. ***$p < 0.001$, ****$p < 0.0001$, $n = 3$. (H) Western blotting analysis of Gpx4 in 4T1 cells upon treatments by PBS, C–N, Ce6 and C–N–Ce6 under hypoxia or laser condition respectively. (I) Immunofluorescence microscopy of HMGB1 release from the nuclei to the cytosol in 4T1 cells. Scale bar: 50 μm. (J) Immunofluorescence microscopy of CRT exposure on the cell surface of 4T1. Scale bar: 50 μm. (For interpretation of the references to colour in this figure legend, the reader is referred to the Web version of this article.)

treatments without laser irradiation were set as control, where no hypoxia environment was observed as shown in Fig. S5. Thus, it could speculate the PDT could not only catalyze ROS-generation reaction but also promote GSH-depletion depolymerization of C–N–Ce6 micelles by aggravating hypoxia. Simultaneously, the membrane potential of mitochondria was evaluated by JC-1 dye to assay the function of mitochondria as Fig. 5E. We could find that the ratio of Red/Green fluorescence obviously decreased in Ce6, C–N–Ce6 and the positive control CCCP groups, indicating the loss of membrane potential and later the profound damage in mitochondria, while the blank nanoreactor could also slightly impact the membrane potential. Ferroptosis probe C11-BODIPY was normally adopted to detect the level of lipid peroxides according to previous report [19]. Hence, C11-BODIPY was adopted here to determine whether the degree of ferroptosis was enhanced. As shown in Fig. 5F, the cells in C–N–Ce6 group displayed higher green fluorescence when treated with NIR laser irradiation compared to the group without laser treatment, which displayed 1.27-folds higher than that in Ce6 group. Therefore, the C–N–Ce6 group receiving laser treatment demonstrated severe ferroptosis than that in Ce6 group when under laser irradiation, which may be aided by the PDT related hypoxia-targeted enhancement of ferroptosis. The combinational effect of ROS-generator Ce6 and GSH-depletion C–N was learned by physical mixture of them. Cell apoptosis analysis was done via FITC Annexin V Apoptosis Detection Kit with 7-AAD and measured by flow cytometry. As displayed in Fig. S6, C–N alone didn't influence the cell viability, while the physical mixture of C–N and Ce6 evidently increased the apoptosis ratio relative to sole Ce6.

Ulteriorly, western blotting was done to evaluate the expression of Gpx4, a main regulator in the ferroptosis process owning to its unique function in reducing complex hydroperoxides [20]. The expression of Gpx4 was evaluated under two conditions. Firstly, cells were treated with PBS, C–N, Ce6 and C–N–Ce6 respectively, which later received laser irradiation to preform PDT and the companied hypoxia. As shown in Fig. 5H, similar tendency could be observed compared with the C11-BODIPY staining. The levels of Gpx4 in free Ce6 and C–N–Ce6 was lower than that in control and C–N group, in which PDT would not function without the photosensitizer. Satisfactory, the level of Gpx4 was the lowest in C–N–Ce6, which further verified the hypoxia-targeted enhancement of ferroptosis of C–N–Ce6. Afterwards, $CoCl_2$ was adopted to create hypoxia intracellular environment. The blank micelle C–N and C–N–Ce6 alone can response to hypoxia environment and catalyzed by NTR enzyme, the GSH-depletion process would happen in the meanwhile. The ruined redox homeostasis would in turns impact the expression of Gpx4. Hence, we could discover that the expression of Gpx4 in C–N and C–N–Ce6 group was decreased compared with the control group, indicating the hypoxia-aided Gpx4 modulation ability of C–N and C–N–Ce6. GSH and Vitamin E, inhibitors of ferroptosis, were utilized here to verify ferroptosis was a part of reason in cell death. As shown in Fig. S7, GSH and Vitamin E both could partly reverse the C–N–Ce6-induced cytotoxicity, confirming ferroptosis occurs during the treatment.

### 3.8. ICD-inducing effect of C–N–Ce6

Ferroptosis is recognized as a programmed cell death (PCD), mainly resulting from accumulation of lipid peroxidation products (LPO). It has been reported that PDT could elicit ICD, which could initialize immune response and later cancer therapy. Simultaneously, ferroptosis could evoke ICD by releasing "find me" signal, including lipid mediators and (High Mobility Group Box 1) HMGB1, with the potential to activate immune response. Here, the ability of Ce6 and C–N–Ce6 in inducing ICD was evaluated. As displayed in Fig. 5I, we could observe the exposure of HMGB1 from nucleus with the treatment of Ce6 and C–N–Ce6. More specifically, a considerable part of HMGB1 still located in nucleus compared with C–N–Ce6 group, where no obvious HMGB1 was observed in nucleus. Similarly, the exposure of CRT could also be seen in Ce6 and C–N–Ce6 groups as exhibited in Fig. 5J, proving the great potential of C–N–Ce6 as immune-generator.

### 3.9. In vivo distribution assay

The fluorescence property of Ce6 endowed the as-prepared C–N–Ce6 with a fluorescence signal, which was utilized to track the distribution of C–N–Ce6 by itself. Free Ce6 and C–N–Ce6 were intravenously injected into mice bearing 4T1 orthotopic mammary tumors. Here the real-time performance of Ce6 and C–N–Ce6 was monitored by a Maestro in vivo imaging system. As shown in Fig. 6A, the fluorescence of Ce6 in C–N–Ce6 group was much stronger than that in Ce6 group, which lasted in the entire distribution process. Semiquantitative results in Fig. 6B revealed same tendency, where the MFI of Ce6 in C–N–Ce6 group at tumor region was much higher than that in Ce6 group during 24 h past administration, further indicating better tumor enrichment of C–N–Ce6 was achieved than free Ce6. Simultaneously, the fluorescence of Ce6 in Ce6 group continuously decreased within 24 h, which was similar in C–N–Ce6 group, but the fluorescence of Ce6 was slightly higher in 4 h past administration than 2 h, which offered guidance for determining the time for laser irradiation during PDT therapy. After 24 h, the mice were executed, major organs and tumors were collected and imaged by the in vivo imaging system. Superior fluorescence intensity in tumor session was observed in C–N–Ce6 group than that in Ce6 as displayed in Fig. 6C, which was consist with the results of Fig. 6A. Semiquantitative results were displayed as Fig. 6D, the MFI of Ce6 in C–N–Ce6 was 2.13-folder higher than that in Ce6 group. Furthermore, the excised tumor masses were subjected to frozen section, the acquired tumor sessions were stained with DAPI and imaged by confocal microscope. It was inferred from Fig. 6E that C–N–Ce6 possessed better tumor penetration ability than Ce6, which may contribute to more satisfactory therapeutic outcomes.

### 3.10. In vivo antitumor assay

The potential of C–N–Ce6 for antitumor therapy was evaluated in 4T1 breast tumor mice. The tumor growth curve after treatment is exhibited in Fig. 7A. As expected, the final preparation C–N–Ce6 displayed the highest tumor inhibition rate, which was measured to be 73.66%, much higher at of C–N (11.92%), Ce6(32.95%) and C–N + Ce6(46.70%) groups. It is surprising that the C–N + Ce6 had superior tumor inhibition rate to that of Ce6 group, which may be resulted from the hypoxia-activated destruction of the C–N and the accompanying GSH depletion, leading to anabatic ferroptosis. Owning to the relatively poor distribution of Ce6 and the lack of GSH-depletion ability, the therapeutic effect of Ce6

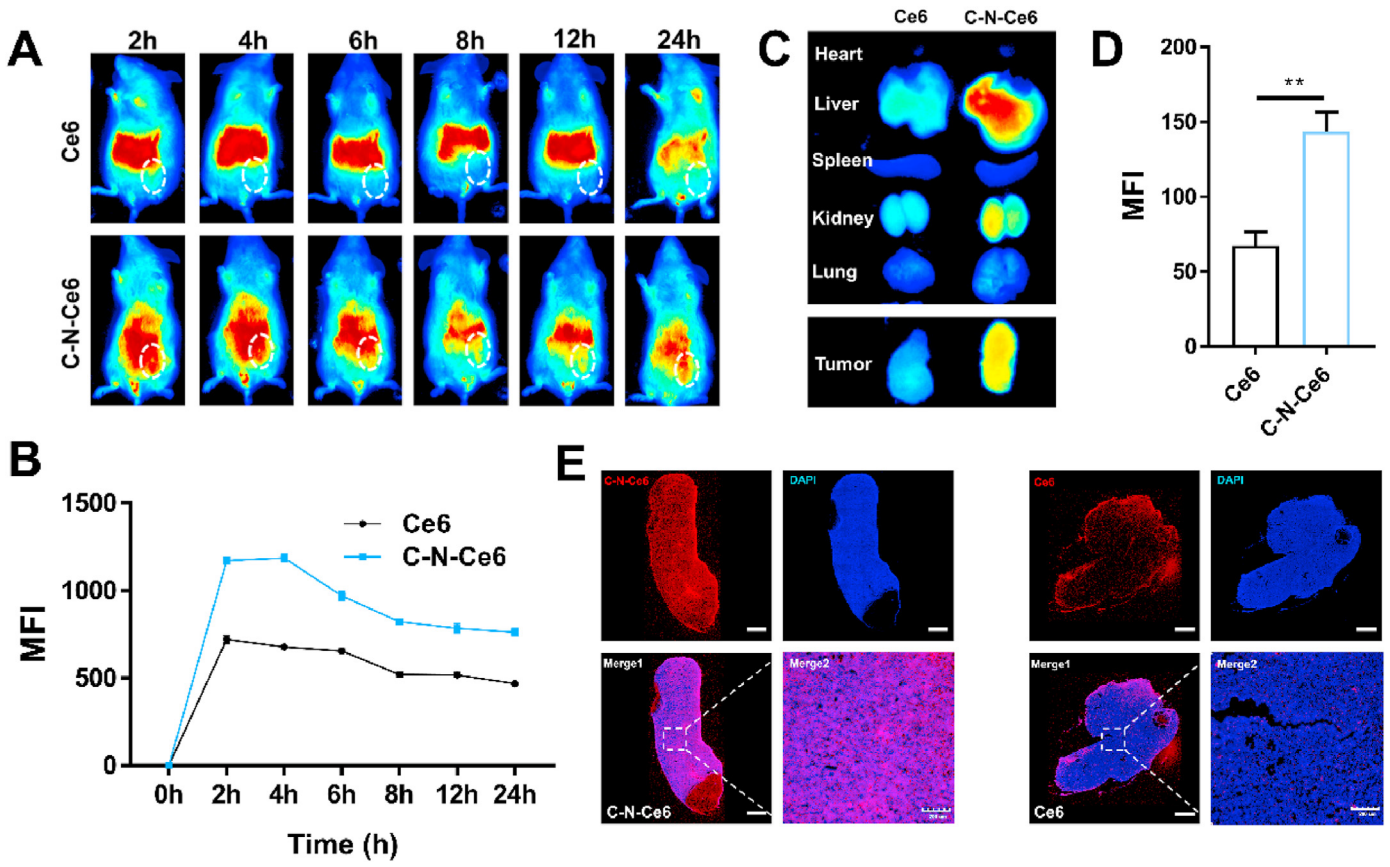


**Fig. 6.** In vivo distribution assay of C–N–Ce6 and immunofluorescence assays for tumor samples. (A) Fluorescence images of Ce6 and C–N–Ce6 distribution on breast tumor bearing mice in vivo at designed time intervals. (B) Semi-quantitative analysis of fluorescence intensity in tumor regions during the distribution process by Maestro 2.10.0 software. (C) Fluorescence images of Ce6 and C–N–Ce6 distribution on dissected tumor masses and other organs. (D) Semi-quantitative analysis of fluorescence intensity in tumor by Maestro 2.10.0 software. **$p < 0.01$, $n = 3$. (E) Distribution patterns of Ce6 and C–N–Ce6 in tumor slices, red fluorescence represented Ce6, blue means cell nucleus in tumor masses. Scale bar: 1200 μm. (For interpretation of the references to colour in this figure legend, the reader is referred to the Web version of this article.)

group was more inferior to that of C–N–Ce6 group, reminding the potential of the combinational strategy. In the meanwhile, the weights of mice were also monitored every two days as shown in Fig. 7B, all groups showed comparable tendency in body weights compared with the control group, verifying promising low systemic toxicity and good biocompatibility in vivo. After the treatment, the tumors of different groups were excised and weighted as shown in Fig. 7C, which was similar with the results in Fig. 7A. The tumors of C–N–Ce6 group were of the minimum weights, displaying the best tumor suppression efficiency. The tumor suppression rates were 7.00%, 19.08%, 35.90%, 60.67% in C–N, Ce6, C–N + Ce6 and C–N–Ce6 groups respectively. Tumor growth curves were monitored as Fig. 7D of individual groups, which could specifically explain the tendency of Fig. 7A. Similarly, C–N–Ce6 showed the best tumor inhibitory ability. The HE results of the tumors were used to observe the pathological characteristics of the tumor tissue, as shown in Fig. 7E, where large areas of necrotic tumor cells could be seen in the tumors from the C–N–Ce6 group.

In addition, HE staining of other organs was performed as shown in Fig. S8. Slides of the major organs from nanoparticle-treated mice did not show obvious abnormalities or lesions compared to those in the Control group, indicating a lack of assessable organ damage and the good biocompatibility of the prepared nanoparticles.

Furthermore, tumor slices were subjected to histological section assessment by Tunel assay, which was used to identify and quantify apoptotic cells. As illustrated in Fig. 7E, C–N–Ce6 had the most apoptotic tumor cells, semi-quantitative analysis of the positive Tunel cells was displayed as Fig. 7F, where tumor sessions in C–N–Ce6 group showed nearly 32.26% area of positive Tunel cells compared to Control (0.97%), C–N (3.79%), Ce6 (9.97%) and C–N + Ce6(25.20%) groups separately.

### 3.11. Immune response in tumor

As we verified above, Ce6 and the final preparation Ce6–C–N could induce ICD when exposing to laser irradiation, including CRT exposure and HMGB1 release. Thus, the immune environment in tumor after therapy was evaluated, including the ratio of T cells, DC cells and immunosuppressive cells. Firstly, the amounts of $CD206^{+}F4/80^{+}$ M2 polarized macrophages were detected in Fig. 8A. We could figure out that Ce6 itself slightly decreased the ratio of macrophages (8.74%) in tumors compared to control group (8.49%), while the final preparation C–N–Ce6 showed inhibitory effect on the immunosuppressive environment, where the ratio of M2 macrophages was obviously decreased, measuring to 5.77%. Simple physical mixture of C–N and Ce6 didn't reach satisfactory outcomes (8.18%) compared with the chemical conjugation. In the meanwhile, $CD11b^{+}Gr\text{-}1^{+}$ MDSCs were also measured as Fig. 8B. Similarly, the C–N–Ce6 dramatically decreased the ratio of MDSCs from 18.65% (Control group) to 9.97%, which was superior than that of C–N (17.23%), Ce6 (15.92%) and the mixture (15.09%), proving its function in inhibiting immunosuppressive environment. Apart from that, the $CD3^{+}$ T cells, $CD3^{+}CD4^{+}$ T cells and $CD3^{+}CD8^{+}$ T cells were evaluated as displayed in Fig. 8C, which possessed anti-tumor immunity. Obviously, C–N–Ce6 remarkable promoted the activation of $CD3^{+}$ T cells, which

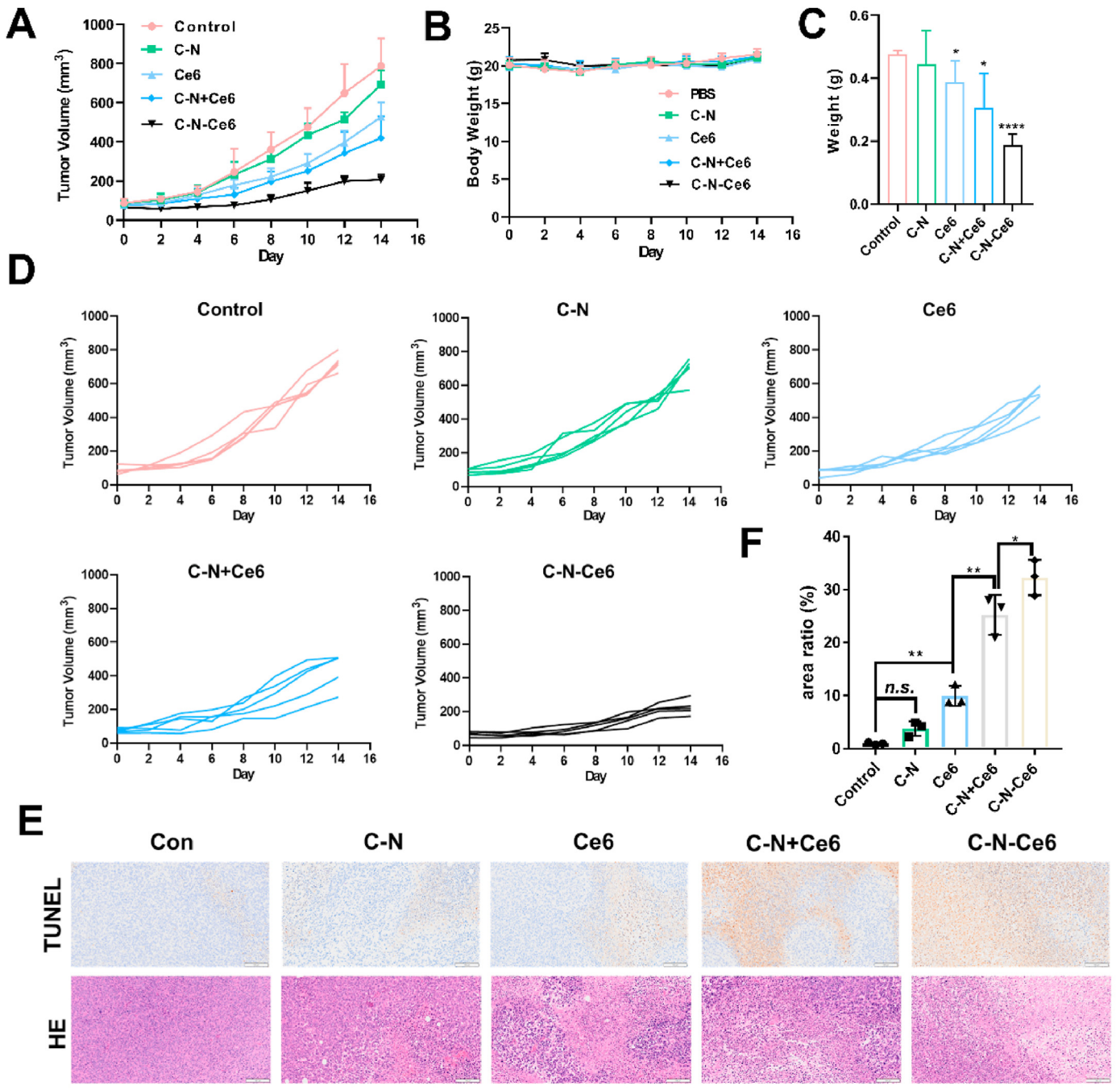


**Fig. 7.** In vivo antitumor efficacy evaluation. (A) Tumor growth curve of the 4T1tumor-bearing mice with PBS, C–N, Ce6, C–N + Ce6 and C–N–Ce6 treatment. (B) Weights of mice monitored every two days during drug treatment. (C) Weights of excised tumor masses of different groups. (D) Tumor growth curve of the 4T1tumor-bearing mice of distinct groups. (E) HE staining and Tunel assay were employed in dissected tumor masses of different drugs treatment. Scale bar: 100 μm. (F) Semi quantitative results of Tunel positive cells (area ratio) in image E, *$p < 0.05$, **$p < 0.01$, $n = 3$.

were measured to be 21.41%, much higher than that of C–N (14.76%), Ce6 (12.83%) and the mixture (17.82%). The ratio of $CD3^+CD4^+$ T cells and $CD3^+CD8^+$ T cells in C–N–Ce6 groups was 1.21% and 3.59% separately, reaching the highest among all the groups. The activity of DC cells was measured in Fig. 8D, which was consistent with above results. The $CD11c^+CD80^+CD86^+$ DC cells in C–N–Ce6 group were the highest, reaching 7.58%, which was much higher than control group (2.35%), while C–N and Ce6 could also slightly increase the ratio, which may be attributed to the ICD-inducing ability of Ce6 and the adjuvant effect of the oligosaccharide chitosan.

## 4. Conclusion

The NADPH-consuming micelles are specially designed here, which could collaborate with the ROS generating photodynamics therapy (PDT) by depleting intracellular GSH and thioredoxin under hypoxia condition, resulting in ruined redox homeostasis and the final cascade amplified ferroptosis. The tailored micelle was briefly prepared by conjugating hypoxia-sensitive segment p-nitrobenzyl chloroformate (PNZ-Cl) to the hydrophilic chitosan (CS), the resulting micelle was further modified with photosensitizer Ce6 via PEG linkage. When receiving laser irradiation, the photosensitizer would generate ROS and consume oxygen in the

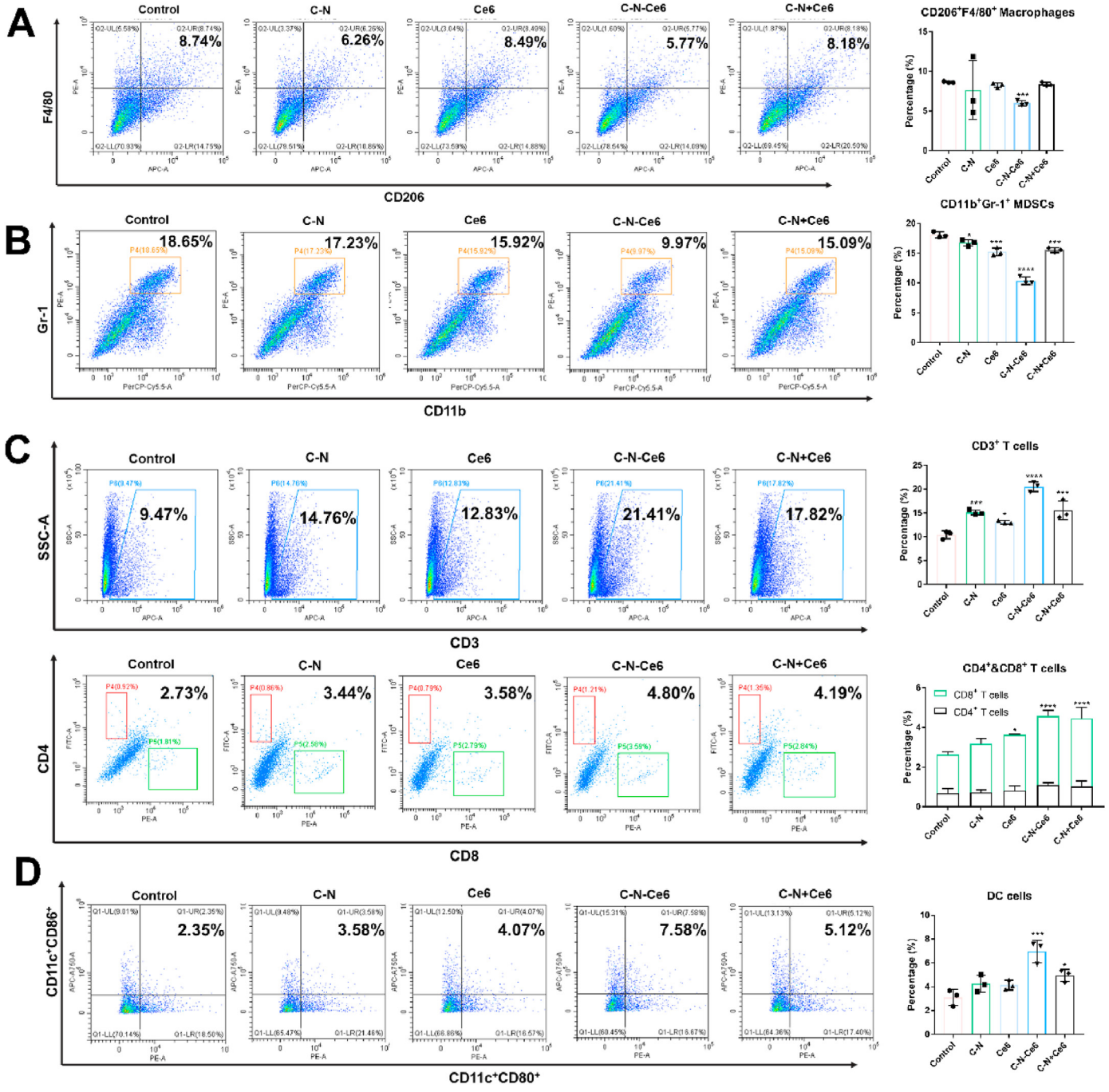


**Fig. 8.** In vivo Immune response in tumor. (A) The ratio of CD206+F4/80+ macrophages in tumors of Control, C–N, Ce6, C–N + Ce6 and C–N–Ce6 groups. (B) The ratio of CD11b + Gr-1+ MDSCs in tumors of Control, C–N, Ce6, C–N + Ce6 and C–N–Ce6 groups. (C) The ratio of $CD3^+$ T cells, $CD3^+CD4^+$ T cells and $CD3^+CD8^+$ T cells in tumors of Control, C–N, Ce6, C–N + Ce6 and C–N–Ce6 groups. (D) The ratio of $CD11c^+CD80^+$ $CD86^+$MDSCs in tumors of Control, C–N, Ce6, C–N + Ce6 and C–N–Ce6 groups.

meanwhile. The resulting anabatic hypoxia in turns promote the NTR-catalyzed electron-accepting response of micelles, with evidently enhanced NADPH consumption and ultimately ruined redox homeostasis, contributing to cascade amplified ferroptosis with robust ROS. Most importantly, the accompanied immunogenic cell death (ICD) and releasing danger-associated molecular patterns (DAMPs) could boost dendritic cells (DCs) maturation and the subsequent T-cell-mediated profound immune response. The work excavates the other biochemical reaction during the hypoxia-sensitive process of C–N–Ce6 by diminishing intracellular GSH and thioredoxin, providing a candidate of ferroptosis inducers against solid tumors.

## Credit author statement

**Fangying Yu**: Conceptualization, Methodology, Formal analysis, Investigation, Data curation, Writing – original draft, Writing – review & editing. **Xuwei Shang**: Conceptualization, Methodology, Validation, Writing – review & editing. **Zixu Wang**: Methodology, Writing – review & editing. **Yun Zhu**: Methodology, Writing – review & editing. **Simin Chen**: Formal analysis, Writing – review & editing. **Hong Yuan**: Resources, Supervision, Project administration, Funding acquisition cquisition. **Fuqiang Hu**: Conceptualization, Resources, Writing – review & editing, Supervision, Project administration, Funding acquisition.

## Declaration of competing interest

The authors declare that they have no known competing financial interests or personal relationships that could have appeared to influence the work reported in this paper.

## Data availability

The authors are unable or have chosen not to specify which data has been used.

## Acknowledgement

The work was supported by Zhejiang Provincial Natural Science Foundation of China under Grant No. D19H300001. We thank Linzhao Xiaonan from the core facility platform of Zhejiang University School of Medicine for their technical support. We thank Lijuan Mao from the Analysis Center of Agrobiology and Environmental Science, Zhejiang university.

## Appendix A. Supplementary data

Supplementary data to this article can be found online at https://doi.org/10.1016/j.mtbio.2022.100532.

## References

[1] J.Y. Cao, S.J. Dixon, Mechanisms of ferroptosis, Cell. Mol. Life Sci. 73 (11–12) (2016) 2195–2209.
[2] S.J. Dixon, B.R. Stockwell, The Hallmarks of Ferroptosis 3 (1) (2019) 35–54.
[3] X. Song, X. Wang, Z. Liu, Z. Yu, Role of GPX4-mediated ferroptosis in the sensitivity of triple negative breast cancer cells to gefitinib, Front. Oncol. 10 (2020), 597434.
[4] J. Ni, K. Chen, J. Zhang, X. Zhang, Inhibition of GPX4 or mTOR overcomes resistance to Lapatinib via promoting ferroptosis in NSCLC cells, Biochem. Biophys. Res. Commun. 567 (2021) 154–160.
[5] S.C. Wang, Y.Y. Lu, K. Woods, G. Di Trapani, K.F. Tonissen, Investigating the thioredoxin and glutathione systems' response in lymphoma cells after treatment with [Au(d2pype)2]Cl, Antioxidants-Basel 10 (1) (2021).
[6] M. Jovanovic, A. Podolski-Renic, M. Krasavin, M. Pesic, The role of the thioredoxin detoxification system in cancer progression and resistance, Front. Mol. Biosci. 9 (2022), 883297.
[7] R. Kumari, D. Sunil, R.S. Ningthoujam, Hypoxia-responsive nanoparticle based drug delivery systems in cancer therapy: an up-to-date review, J. Contr. Release 319 (2020) 135–156.
[8] J. Lippmann, K. Petri, S. Fulda, J. Liese, Redox modulation and induction of ferroptosis as a new therapeutic strategy in hepatocellular carcinoma, Transl Oncol 13 (8) (2020), 100785.
[9] Z. Zhou, J. Song, L. Nie, X. Chen, Reactive oxygen species generating systems meeting challenges of photodynamic cancer therapy, Chem. Soc. Rev. 45 (23) (2016) 6597–6626.
[10] R. Alzeibak, T.A. Mishchenko, N.Y. Shilyagina, I.V. Balalaeva, M.V. Vedunova, D.V. Krysko, Targeting immunogenic cancer cell death by photodynamic therapy: past, present and future, J Immunother Cancer 9 (1) (2021).
[11] W. Li, J. Yang, L. Luo, M. Jiang, B. Qin, H. Yin, C. Zhu, X. Yuan, J. Zhang, Z. Luo, Y. Du, Q. Li, Y. Lou, Y. Qiu, J. You, Targeting photodynamic and photothermal therapy to the endoplasmic reticulum enhances immunogenic cancer cell death, Nat. Commun. 10 (1) (2019) 3349.
[12] F. Yu, X. Shang, Y. Zhu, H. Lou, Y. Liu, T. Meng, Y. Hong, H. Yuan, F. Hu, Self-preparation system using glucose oxidase-inspired nitroreductase amplification for cascade-responsive drug release and multidrug resistance reversion, Biomaterials 275 (2021), 120927.
[13] Y.W. Hu, Y.Z. Du, N. Liu, X. Liu, T.T. Meng, B.L. Cheng, J.B. He, J. You, H. Yuan, F.Q. Hu, Selective redox-responsive drug release in tumor cells mediated by chitosan based glycolipid-like nanocarrier, J. Contr. Release 206 (2015) 91–100.
[14] X. Jing, F. Yang, C. Shao, K. Wei, M. Xie, H. Shen, Y. Shu, Role of hypoxia in cancer therapy by regulating the tumor microenvironment, Mol. Cancer 18 (1) (2019) 157.
[15] G. Yang, Y. Liu, J. Teng, C.X. Zhao, FRET ratiometric nanoprobes for nanoparticle monitoring, Biosensors 11 (12) (2021).
[16] P. Zou, H. Chen, H.J. Paholak, D. Sun, Noninvasive fluorescence resonance energy transfer imaging of in vivo premature drug release from polymeric nanoparticles, Mol. Pharm. 10 (11) (2013) 4185–4194.
[17] C. Wang, M. Han, X. Liu, S. Chen, F. Hu, J. Sun, H. Yuan, Mitoxantrone-preloaded water-responsive phospholipid-amorphous calcium carbonate hybrid nanoparticles for targeted and effective cancer therapy, Int. J. Nanomed. 14 (2019) 1503–1517.
[18] X. Qin, M. Zhang, X. Hu, Q. Du, Z. Zhao, Y. Jiang, Y. Luan, Nanoengineering of a newly designed chlorin e6 derivative for amplified photodynamic therapy via regulating lactate metabolism, Nanoscale 13 (27) (2021) 11953–11962.
[19] J. Yang, S. Ma, R. Xu, Y. Wei, J. Zhang, T. Zuo, Z. Wang, H. Deng, N. Yang, Q. Shen, Smart biomimetic metal organic frameworks based on ROS-ferroptosis-glycolysis regulation for enhanced tumor chemo-immunotherapy, J. Contr. Release 334 (2021) 21–33.
[20] X. Sui, R. Zhang, S. Liu, T. Duan, L. Zhai, M. Zhang, X. Han, Y. Xiang, X. Huang, H. Lin, T. Xie, RSL3 drives ferroptosis through GPX4 inactivation and ROS production in colorectal cancer, Front. Pharmacol. 9 (2018) 1371.